Series of M_xWO_3/ZnO (M = K, Rb, NH_4) nanocomposites: Combination of energy saving and environmental decontamination functions

Xiaoyong Wu [a], Junting Wang [a], Gaoke Zhang [a,*], Ken-ichi Katsumata [b], Kazumichi Yanagisawa [c], Tsugio Sato [d], Shu Yin [d,*]

[a] Resource and Environmental Engineering, Wuhan University of Technology, 122 Luoshi Road, Wuhan, Hubei, China
[b] Photocatalysis International Research Center, Research Institute for Science and Technology, Tokyo University of Science, Japan
[c] Research Laboratory of Hydrothermal Chemistry, Faculty of Science, Kochi University, Japan
[d] Institute of Multidisciplinary Research for Advanced Materials, Tohoku University, 2-1-1, Katahira, Aoba-ku, Sendai 980-8577, Japan

ABSTRACT

Series of new M_xWO_3/ZnO (M = K, Rb, NH_4) nanocomposites were successfully prepared by simple two-steps method in a mild condition. The as-prepared M_xWO_3/ZnO composite films showed nice UV light blocking, VIS light transmittance and NIR light shielding properties. Furthermore, the optical properties of the composites could be tuned by adjusting the M_xWO_3 content and film thickness. Particularly, the Rb_xWO_3/ZnO with small amounts of Rb_xWO_3 contents exhibited the promising optical properties and also excellent thermal stability. From the practical application viewpoint, the simulated experiment found that the simulated house decorated with sample film as smart window presented nice NIR light induced heat insulation for energy saving, and the Rb_xWO_3/ZnO decorated one was even better than that of ITO. In addition, both the powder and film samples displayed high continuously toxic NO gas decomposing ability under the UV light irradiation. The mechanisms for the multifunctionality of the samples were related to the polaron transition, localized surface plasma resonance (LSPR) and suitable band gaps. Therefore, the new M_xWO_3/ZnO composites and relevant films not only showed promising harmful UV light absorption, high VIS light brightness, excellent NIR light induced heat insulation, but also nice toxic NO gas photodecomposition property, indicating their brilliant prospect in both of energy saving and environmental cleanup.

© 2016 Elsevier B.V. All rights reserved.

1. Introduction

Energy depletion and environmental pollution have become two urgent problems in modern time. In this case, the researches about how to save energy and alleviate the environmental contamination reasonably turn out to be the hot topics [1–5]. As for the energy saving, development of nanomaterials as smart coating to control natural solar light utilization has been paid particular attention in the recent [6–8]. It is well-known that the natural solar light consisted of three types of radiation, ultraviolet radiation (UV, <380 nm, 5%), visible light (VIS, 400–780 nm, 45%) and near-infrared radiation (NIR, 780–2500 nm, 50%). Among them, the UV light is well-recognized to be the harmful radiation for human body; the VIS light is utilized for the brightness of room in daytime and the NIR light is perceived as the original source for heat energy

in our daily life [9,10]. Every year, great amounts of energy are consumed, typically for air conditioners and fans, to keep building and vehicle temperature comfortably, caused by the NIR light of natural solar light irradiation [11]. Accordingly, it is very essential to develop a material as smart coating for natural solar light control, which can not only transmit majority of VIS light, but also blocking most of UV and NIR light. In this case, this type of smart coating is possible to depress the indoor temperature increment and remove the adverse effect of UV light as well as keeping nice inner brightness under the strong summer natural solar light irradiation, while in winter it can also hinder the energy loss from warm indoor by heat insulation, finally achieving energy saving and also reducing the emission of carbon dioxide [12].

Over the past few decades, some materials, e.g. black compounds, noble metals, rare-earth hexaborides, tin-doped indium oxide (ITO), etc., have been proposed to fulfil the aforementioned multifunctionality for natural solar light control [13–16]. However, all of them have their own drawbacks such as low VIS transmittance, high cost, relatively poor NIR light shielding capability,

expensive device or complex fabrication process, etc. [17]. Hexagonal tungsten bronzes, M_xWO_3 (M = Rb, K, Cs, NH_4), have recently drawn lots of attention as one of new functional materials for solar light control due to its excellent NIR light blocking performance and high VIS light brightness, which have been widespread applied in smart windows, gas sensors, electrochromic materials, photocatalysts, military weapon and cancer therapy [18–21]. However, from the viewpoint of practical applications, the VIS light transmittance and UV light blocking properties of hexagonal tungsten bronzes also requires further improvement owing to their relative narrow band gap (2.5–3 eV).

On the other hand, owing to the construction of modernization, the air pollution and haze phenomena have turned out to be more and more serious especially in recent China. In this case, how to alleviate and clean air contamination has become extremely urgent problem. Photocatalysis, as a green chemical method, has attracted great amount of interests for improving air conditions due to its energy saving, high efficiency and environmental-friendly. Accordingly, lots of photocatalysts such as TiO_2, ZnO, ZnS and $SrTiO_3$ and so on have been developed [22–24]. Particularly, ZnO not only present nice photocatalytic performance, but also exhibit excellent VIS light transmittance and UV light shielding properties.

However, until to now, few efforts have been made to investigate the materials for combination of energy saving and environmental cleanup functions together. In our previous work [25], we have successfully combined the excellent NIR light absorbing materials Cs_xWO_3 with ZnO photocatalyst to form a composite as smart coating materials, which not only shield NIR and UV lights but also keep nice VIS light transmittance as well as presenting outstanding toxic gas decomposing performance. Nevertheless, this kind of functional composite is just a preliminary work, and the comprehensive and deep insight researches are still lack. For instance, whether it is possible to combine other NIR light shielding materials with ZnO to achieve the same multifunctionality and then form a system. How about the effect of different factors, e.g. working temperature, coating thickness, component ratio, etc. More importantly, the detailed mechanism for multifunction is demand to be clarified. In addition, Cs source in earth is rarer compared with those of K, Rb, NH_4. So from the viewpoint of practical application and fundamental research, the more detailed and comprehensive research about other series of composites are still urgently required to fulfil energy saving and environmental cleanup simultaneously.

Herein, series of M_xWO_3/ZnO (M = K, Rb, NH_4) composites have been prepared by solvothermal method coupled with soft chemical reaction to achieve heat insulation, air decontamination, harmful UV light blocking and high VIS light transmittance simultaneously. The effects of working temperature, coating thickness and component composition on the properties of composites have been investigated. What's more, the detailed mechanism for NIR light shielding, UV light blocking, VIS light transmittance as well as photocatalysis has been discussed.

2. Experimental

2.1. Sample preparation

2.1.1. Preparation of K_xWO_3 nanorods

The K_xWO_3 nanorods were prepared according to our previous work [26] with a little bit improvement as follows: Firstly, 1.63 g K_2WO_4 and 1.74 g K_2SO_4 were dissolved in 50 mL of distilled water under fiercely stirring. Then, the pH value of mixed solutions was adjusted to 1.5 with another 30 mins stirring. After that, the precursor solution was transferred to 100 mL Teflon-lined autoclave and heated at 200 °C for 24 h. Finally, the

as-fabricated particles were post-calcined at 600 °C for 2 h under an H_2 (5 vol%)/N_2 atmosphere.

2.1.2. Preparation of RbxWO3 nanorods

The Rb_xWO_3 nanorods were also prepared according to our previous work [19] with a further reducing treatment as follows: To begin with, 0.2976 g WCl_6 was dissolved into 40 mL dehydrated ethanol with vigorous stirring for 30 mins. Next, 0.052 g RbOH was introduced into the above solution with another 15 mins stirring before adding 10 mL acetic acid. After that, the precursor solution was transferred to 100 mL Teflon-lined autoclave and heated at 240 °C for 20 h. Finally, the as-fabricated particles were post-calcined at 550 °C for 1 h under an H_2 (5 vol%)/N_2 atmosphere.

2.1.3. Preparation of (NH4)xWO3 nanorods

The $(NH_4)_xWO_3$ nanorods were also prepared according to our previous work [9] as follows: First of all, 0.25 g ammonium paratungstate was dissolved into 40 mL ethylene glycol with moderate stirring at 190 °C. After the solution cooling down to the room temperature, 20 mL acetic acid was introduced into the above solution. Then, the precursor solution was transferred to 100 mL Teflon-lined autoclave and heated at 200 °C for 72 h. Finally, the particles were centrifuged, washed and dried in a vacuum at 60 °C overnight.

2.1.4. Preparation of M_xWO_3/ZnO composites

The M_xWO_3/ZnO composites were prepared by a simple soft solution method [25]. In a typical synthesis process, 0.07 g as-synthesized M_xWO_3 particles were dispersed into 80 mL ethanol with sonication for 30 min and magnetically stirring for 30 min. Then, 0.31 g $Zn(CH_3COO)_2 \cdot 2H_2O$ was added into the solution with another 30 min stirring. After that, 20 mL ethanol aqueous solution containing 2 mL distilled water and 0.06 g NaOH were dropwise introduced into the mixed solution with stirring for another 4 h at 85 °C. After cooling down to the room temperature, the final solution was centrifuged, washed and dried at 60 °C overnight. In addition, as representative composite, two more other weight ratios (1:3 and 1:1) of Rb_xWO_3/ZnO were also prepared by the same procedure except for the various masses of Rb_xWO_3 addition. Besides, the pure ZnO was also synthesized by the same process without the addition of M_xWO_3 particles.

2.2. Characterization

The crystalline phases of the specimens were checked by X-ray diffraction (XRD) analysis (Bruker AXS D2 Phaser) with graphite-monochromized CuKα radiation. The morphology and size of the particles were examined by scanning electron microscope (SEM, Hitachi S-4800) and transmission electron microscopy (TEM, JEOLJEM-2010). The elementary mapping and selected area electron diffraction (SEAD) pattern of the composites were carried out by high resolution transmission electron microscopy (HRTEM, FE-TEM, JEM-2100F). The specific surface area was investigated by the BET method (Quantachrome Instruments, NOVA4200e). The atom status of the samples was determined by X-ray photoelectron spectroscopy (XPS, Perkin Elmer PHI 5600). The shift of the binding energy due to the surface state charge was calibrated by using the C 1 s level at 284.6 eV as an internal standard. The transmittance of composite films was obtained by a UV–vis spectrophotometer (Shimadzu, UV-2450), where the product films were prepared as follows: Firstly, the sample powders were dispersed into collodion-ethanol mixed solution with a weight ratio of sample:collodion:ethanol = 0.15:0.93:1.0. Then the solution was magnetically stirred for 24 h fiercely. After the precursor solution prepared, the films were obtained by coating the precursor solution onto a quartz glass by a simple squeegee method. The ITO film
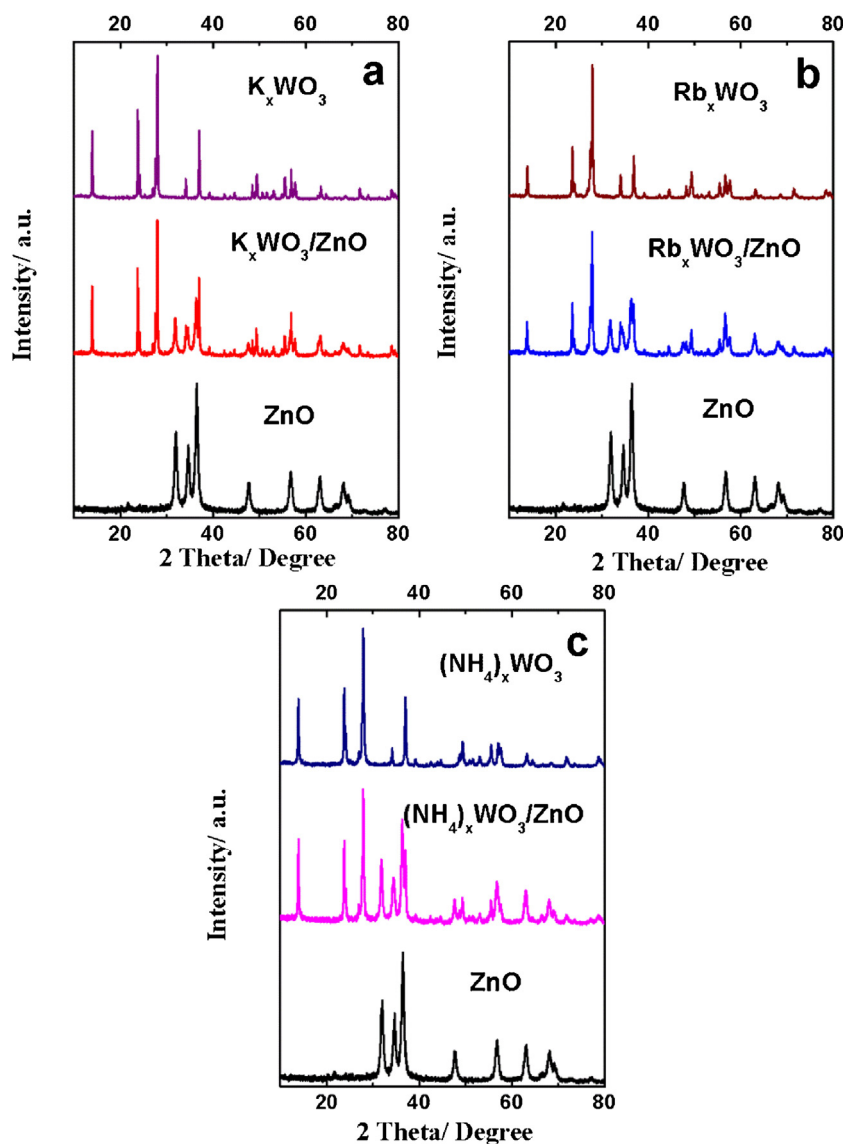
Fig. 1. XRD patterns of composites K_xWO_3/ZnO (a), Rb_xWO_3/ZnO (b), $(NH_4)_xWO_3$/ZnO (c) and their relevant pure substances for ZnO and M_xWO_3 (M = K, Rb, NH_4).

was also fabricated via the same procedure using commercial ITO (10 Ω/□) powder (bought from Mitsubishi Materials Corporation) as precursors. In order to check the effect of film thickness on the properties of composites, the film was also prepared by applicators with different thickness.

2.3. Photocatalytic activity tests

The photocatalytic performance of samples was evaluated by the destruction of continuously toxic NO gas ($deNO_x$) based on a Japanese Standard with the irradiation of a 450 W high pressure mercury lamp at room temperature. Firstly, the sample powder was spread in the hollow (20 mm × 16 mm × 0.5 mm) of a glass plate before placing at the bottom center of the reactor (373 cm^3 of internal volume). Meanwhile, a 1:1 mixed gas consisted of air and nitrogen including 1 ppm of NO was continuously flowed through the reactor with the rate of 200 cm^3 min^{-1}. Before light on, the prepared sample was kept in the dark for 30 min to reach the adsorption and desorption equilibrium of NO gas. After that, every sample was irradiated by the mercury lamp for 10 min, and then another 10 min to recover to the original NO gas concentration

without light irradiation. The concentration of NO gas was checked by a NO_x analyzer (Yanaco, ECL-88A) [27].

3. Results and discussion

XRD analysis was used to check the phase composition and crystallographic structure of the products. Fig. 1 shows the XRD patterns of M_xWO_3/ZnO (M = K, Rb, NH_4) series composites together with the pure one for each component. From Fig. 1, it can be clearly seen that all of the M_xWO_3 presented pure hexagonal tungsten bronze structure with well-known crystal lattice parameters of a = 0.739 nm and c = 0.756 nm without any other characteristic peaks corresponding to impurities observed in profiles. The only difference was the relative peak intensity mainly owing to the various tungsten bronze preparation methods. When M_xWO_3 tungsten bronzes formed composites with ZnO by soft chemical method, the characteristic peaks belonged to M_xWO_3 and ZnO were all exhibited in the composites patterns with the same relative intensity ratios as the single pure ones, respectively. There was also no other impurity peaks appeared, indicating that the simple soft chemical method is feasible to synthesize the pure M_xWO_3/ZnO composites without obvious structure and composition change.
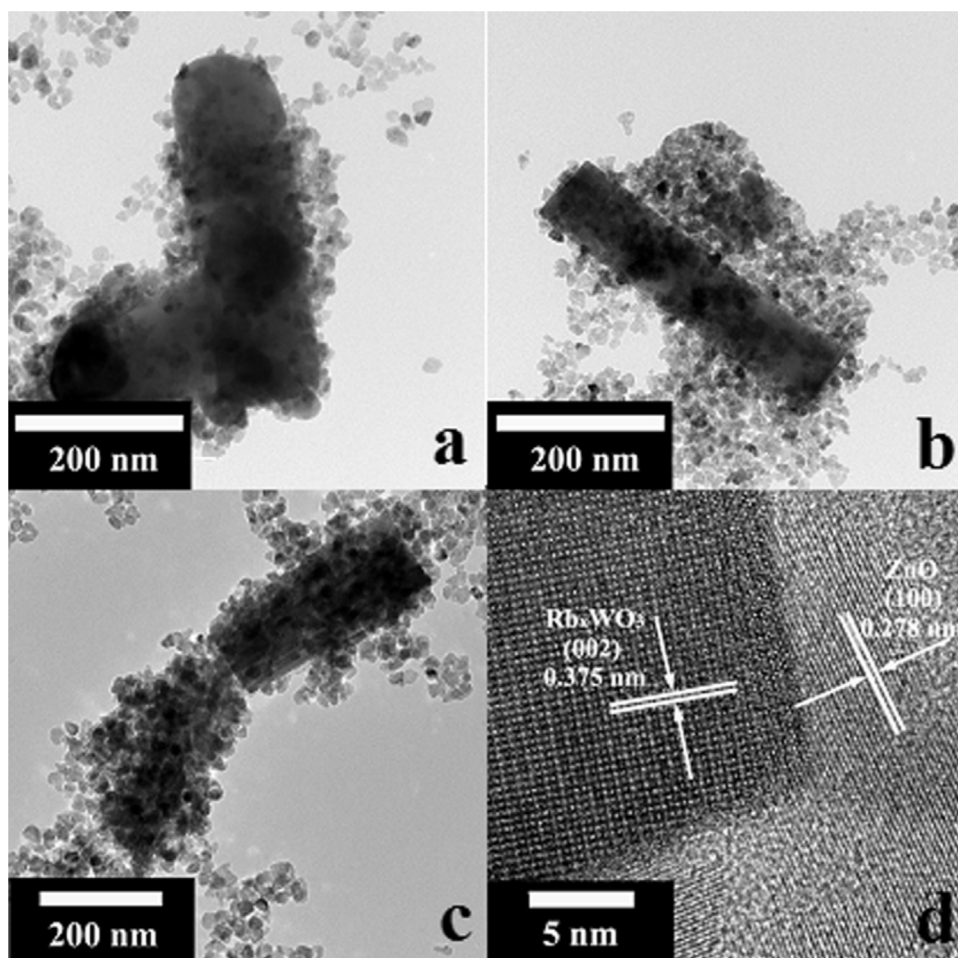
Fig. 2. TEM images of K_xWO_3/ZnO (a), Rb_xWO_3/ZnO (b), $(NH_4)_xWO_3$/ZnO (c) and representative HRTEM image for composite Rb_xWO_3/ZnO (d).
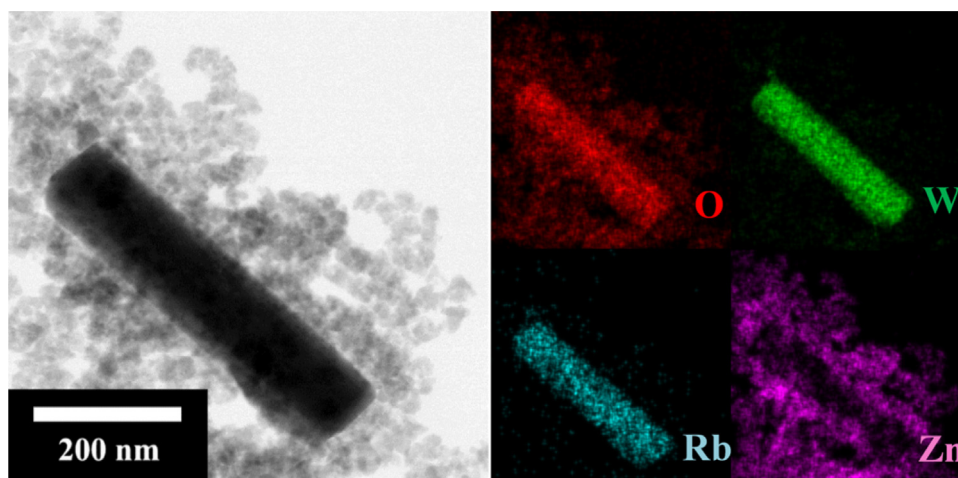

Fig. 3. The representative element mapping images of composite Rb_xWO_3/ZnO with the same scale bar of 200 nm.

Fig. 2 illustrates the TEM images of M_xWO_3/ZnO composites. It is apparent in Fig. 2a–c that the M_xWO_3 particles all demonstrated short nanorod morphology with the length of about 500 nm and the width of 100–200 nm, although three M_xWO_3 were prepared by various aqueous methods as depicted in experimental section, which was beneficial to analyze the property of composites eliminating the effect of particle morphology. In addition, the ZnO small nanoparticles with about 10 nm toughly and randomly

covered on the surface of M_xWO_3 to form composites, which was advantage to fulfil multifunctionality based on each component in composites. The corresponding SEM images of M_xWO_3/ZnO were also appended in Supporting information Fig. A.1. However, probably due to the low concentration of M_xWO_3 rods in the composites of M_xWO_3/ZnO and high coverage density of ZnO nanoparticles on the M_xWO_3, it is hard to find great amounts of clear M_xWO_3/ZnO composites in these images, in which the M_xWO_3 was tightly and
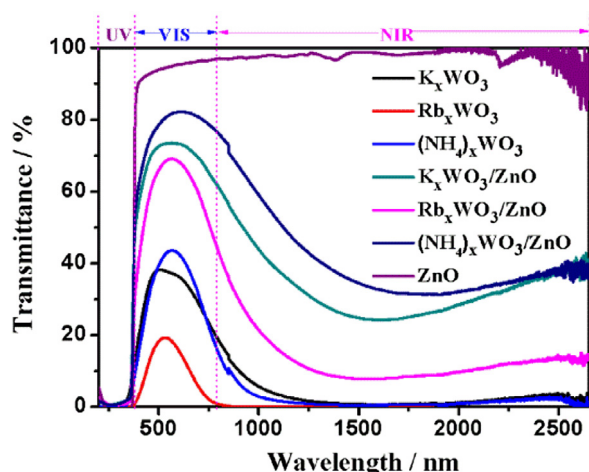
Fig. 4. Transmittance spectra of M_xWO_3/ZnO series film and corresponding pure M_xWO_3 and ZnO ones.

Fig. 5. XPS spectra of W4f spectra of composites K_xWO_3/ZnO (a), Rb_xWO_3/ZnO (b) and $(NH_4)_xWO_3/ZnO$ (c).

intensively covered by ZnO nanoparticles. Generally, the uniformity of the connection of components can affect the properties of the composite (e.g. optical properties and photocatalytic activity, etc.). Nevertheless, in our previous system Cs_xWO_3/ZnO [25], the effect of uniformity connection between two components on the properties of composites was studied, and preliminarily found that there was no big relationship between uniformity connection and properties. So combining this previous study with SEM results, it could be deduced that the connection condition between ZnO and M_xWO_3 in composite possibly played no significant role in the properties of composites. The detailed study about the effect of morphology, contact interface, and contact uniformity on the properties of M_xWO_3/ZnO composites would be our next work. Besides, the representative HRTEM image of Rb_xWO_3/ZnO was also shown in Fig. 2d. It could be confirmed that hexagonal tungsten bronze Rb_xWO_3 and hexagonal wurtzite ZnO were truly existed and formed the as-expected Rb_xWO_3/ZnO composite. What's more, it could be found that the Rb_xWO_3 grew along with the direction of [002], which assigned to the preferable prism growth habit along the c-axis of hexagonal tungsten bronze according to the chemical bonding theory of single crystal growth [28]. In order to further verify the composite composition and structure, the element mapping analysis was employed as shown in Fig. 3. It was obviously viewed that the nanorod consisted of Rb, W and O elements corresponding to Rb_xWO_3 and the surround small nanoparticles comprised of Zn and O elements related to ZnO, which could prove the real formation of Rb_xWO_3/ZnO composite by a soft chemical method.

The optical properties of samples were demonstrated using transmittance spectra of sample films. Fig. 4 presents the transmittance profiles of the films prepared by as-synthesized M_xWO_3, ZnO and M_xWO_3/ZnO composites dispersed in the collodion-ethanol mixed solution. The pure ZnO film presented an outstanding harmful UV light blocking capability due to the wide band gap about 3.2 eV (equaled to 387.5 nm). Moreover, it displayed extremely excellent VIS light transmittance above 92%, which related to its wide band gap. Nevertheless, the NIR light was almost transmittance for ZnO film. As for pure M_xWO_3 films, they could block majority of adversely UV light related to the band gap of 2.98 nm [29]. However, the VIS light transmittance was relatively poor below 50%. What is noteworthy that three M_xWO_3 films all presented strong NIR light shielding property because of their typical hexagonal tunnels structures and mixed valence status, which will be further explained in the following XPS and mechanism sections in details. More importantly, when M_xWO_3 was combined with ZnO to form composites, the M_xWO_3/ZnO composites films

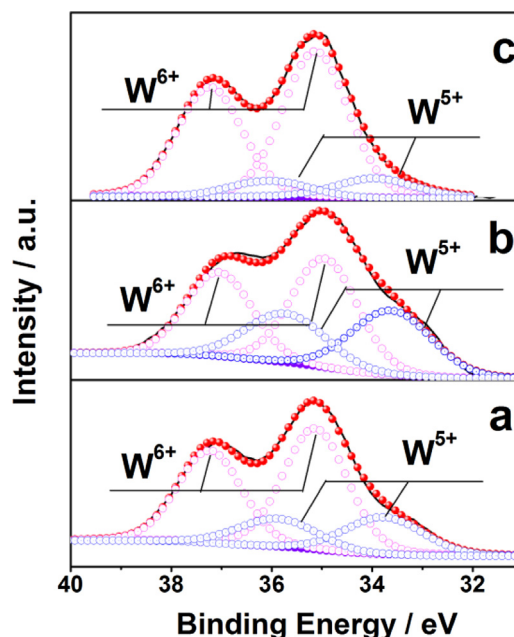inherited the good properties of both M_xWO_3 and ZnO, which all exhibited excellent UV light blocking, relatively good VIS light transmittance and pretty nice NIR light shielding performance. In particular, when Rb_xWO_3 formed composite with ZnO, the film presented much better NIR light shielding capability although the VIS light transmittance was a little bit weaker compared with those of other two composites films, which was mainly related to the amount of W^{5+} ions existed in the hexagonal tungsten bronzes and M concentrations. So in order to confirm this, the XPS analysis was carried out. Fig. 5 shows the XPS spectra of W4f profiles of composites. Three composites all exhibited two groups of fitting peaks. The larger energy group was corresponding to W^{6+} and the smaller energy group was originated from reduced W^{5+}. The difference is that the peak locations of composites K_xWO_3/ZnO (a), $(NH_4)_xWO_3/ZnO$ (c) were situated around 35.1 eV, 37.2 eV for W^{6+} and 33.9 eV, 36.0 eV for W^{5+}, while the composite Rb_xWO_3/ZnO (b) displayed a little bit energy shift to higher energy for these two groups, corresponding to 35.0 eV, 37.1 eV for W^{6+} and 33.7 eV, 35.8 eV for W^{5+} [30,31]. This shift may be owing to the various M ionic radiuses and M incorporating concentrations [25,26,30]. More importantly, it could be clearly learned from Fig. 5 that the composite Rb_xWO_3/ZnO presented much higher ratio of W^{5+}/W^{6+} ions in M_xWO_3 crystal, which is about 0.58, bigger than those of K_xWO_3/ZnO (about 0.35) and $(NH_4)_xWO_3/ZnO$ (about 0.24), indicating much more reduced W^{5+} ions existed in Rb_xWO_3 crystal in comparison of other two composites and also for oxygen vacancies due to the charge compensation. In addition, based on the XPS analysis, the Rb concentration was determined to about 0.3, and K, NH_4 were 0.3, 0.25, respectively. It is well-known that the NIR light shielding property is mainly induced by the existence of reduced W^{5+}, oxygen vacancies and M concentration in hexagonal tungsten bronzes [23–26,30]. So owing to the relatively high W^{5+} ions, oxygen vacancies and M concentration, Rb_xWO_3/ZnO film displayed the best NIR light shielding property among three composites' films as seen in Fig. 4. The detailed mechanism for NIR light shielding will be discussed in the final mechanism section.

Besides, the influence of component content and film thickness on the transmittance property of the representative Rb_xWO_3/ZnO composite film was also investigated. Fig. 6a presented the effect of
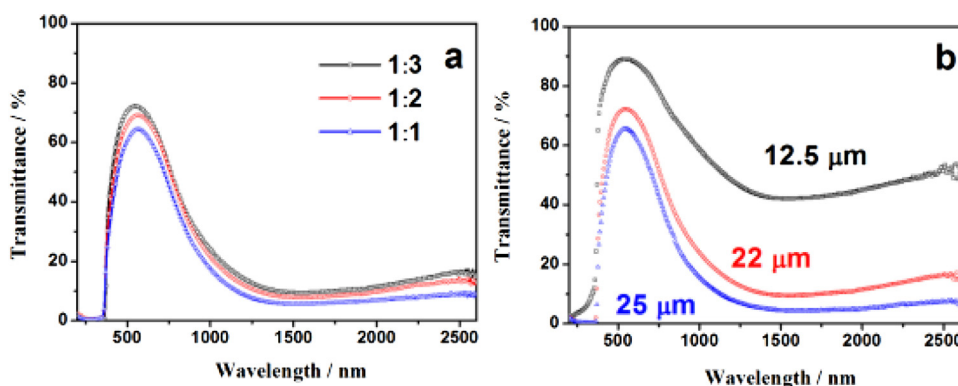
Fig. 6. Transmittance spectra of the representative Rb_xWO_3/ZnO composite film with respect to various weight ratios of Rb_xWO_3 to ZnO (a) and as a function of film thickness (b).
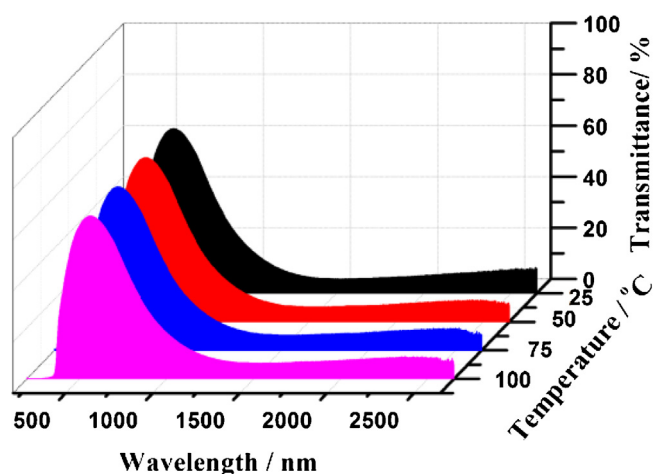
Fig. 7. The dependence of transmittance of representative Rb_xWO_3/ZnO composite film on the time.

weight ratio of Rb_xWO_3 to ZnO on the transmittance performance of samples. It is apparent that with the increment of ZnO content in the composite, the VIS light transmittance increased but NIR light shielding decreased, indicating the ZnO was mainly contributed to the high VIS light transmittance, while Rb_xWO_3 for NIR light insulation. In addition, the effect of film thickness on the optical property of sample film was represented in Fig. 6b. It could be obviously observed that with increasing film thickness, the NIR light shielding property could be significantly improved, however, the VIS light transmittance would decrease inversely. So it could be known that the VIS light transmittance and NIR light shielding properties could be nicely tuned by adjusting weight ratio of components in composite and film thickness. Moreover, the cost of composite film with relatively high NIR light shielding performance could also be significantly reduced with decreasing M_xWO_3 content to 1/3 as compared to that of our previous work with about half of Cs_xWO_3 [25]. In this work, the moderate conditions with 1:2 wt ratio of Rb_xWO_3 to ZnO and 22 μm film thickness were chosen as the representative study target.

Fig. 7 shows the thermal stability of optical property of composite films. It is evidence that with changing temperature from 25 °C to 100 °C, there was no obvious variation observed, implying that the as-prepared composite film has high thermal stability for optical properties. On the other hand, from the viewpoint of practical application, the NIR light shielding capability of sample film was studied by employing a simulated house system using the as-prepared sample film as smart window and then irradiating by NIR light containing light source as presented in Fig. 8a and the

corresponding inner temperature variation with light irradiation time was shown in Fig. 8b. From Fig. 8b, it could be learned that with the elapsing of irradiation time during 60 mins, the temperature in the pure quartz glass decorated house increased about 9 °C from 15 °C to 24 °C, 6.9 °C for ITO one and 4.5 °C for the representative Rb_xWO_3/ZnO composite film one, indicating its excellent IR shielding property of the as-prepared representative Rb_xWO_3/ZnO composite film in this work, demonstrated the optimal heat insulation property followed by ITO one and pure quartz one, which should be due to the excellent NIR light absorption performance of Rb_xWO_3/ZnO composite film in the range of 780 nm to 2500 nm as depicted in Fig. 4.

The photocatalytic activity of samples and relevant films were evaluated by destructing continuously flow NO gas under the irradiation of mercury lamp. Fig. 9 shows the $deNO_x$ ability of the samples in powder and film status, respectively. As seen in Fig. 9A, pure Rb_xWO_3 (a) presented poor $deNO_x$ ability, owing to the small specific surface area about several m^2/g and high recombination rate for photo-generated electron-hole pair. While the pure ZnO (f) exhibited the excellent photocatalytic activity because of the large specific surface area about 85 m^2/g, suitable band gap and relatively low recombination capability, etc. Interestingly, when the M_xWO_3 particles were coupled with ZnO to form composites, three composites K_xWO_3/ZnO (c), Rb_xWO_3/ZnO (b), $(NH_4)_xWO_3$/ZnO (d) all exhibited relatively good $deNO_x$ ability, being much superior to pure Rb_xWO_3 and even being better than that of commercial P25 (e), which should be attributed to the high weight ratio of ZnO about 2/3. In order to verify their practical application, the $deNO_x$ ability of composites' films was also measured in Fig. 9B. It was obvious that all films presented nice photocatalytic activity. More importantly, the composites' film Rb_xWO_3/ZnO and K_xWO_3/ZnO illustrated better performance than that of composite film $(NH_4)_xWO_3$/ZnO, probably assigned to the high crystallinity since the specific surface area of three composites were similar, Rb_xWO_3 and K_xWO_3 have been post-calcined at relatively high temperature as described in experimental section.

Based on the foregoing discussion, it could be concluded that the as-proposed M_xWO_3/ZnO series exhibited nice UV light blocking, VIS light transmittance, NIR light shielding and also showed good photocatalytic activity, indicating their excellent multifunctionality for energy-saving and environmental cleanup as expected. More significantly, the cost and properties of sample films could be easily adjusted by the component content, film thickness and composition.

In order to better understand the multifunctionality performances of the composite films, the possible mechanisms for high NIR light shielding, UV light blocking, VIS light transmittance and excellent photocatalytic property of composites were investigated.
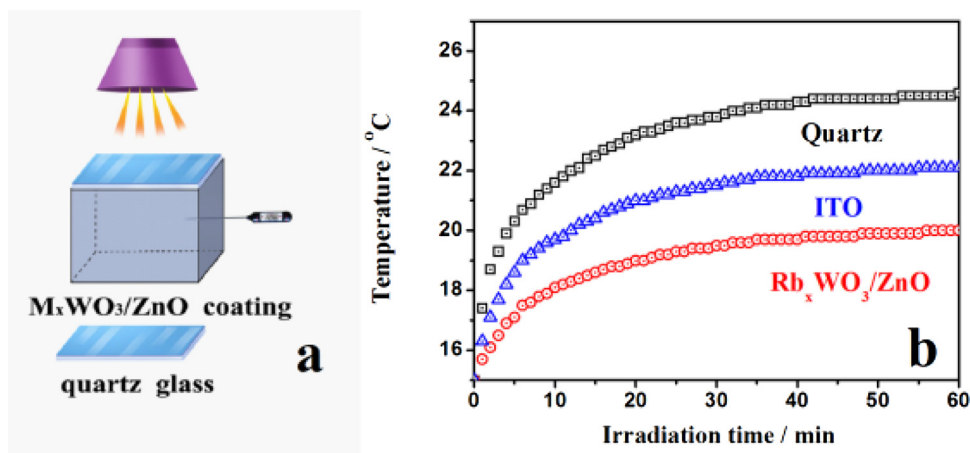
Fig. 8. Schematic illustration of the simulated house decorated with sample film coated quartz glass as smart window under the irradiation of halogen lamp (a) and the dependence of inner temperature of simulated house on the light irradiation time for the pure quartz glass, representative composite Rb_xWO_3/ZnO film coated quartz glass and commercial ITO coated quartz glass (b).
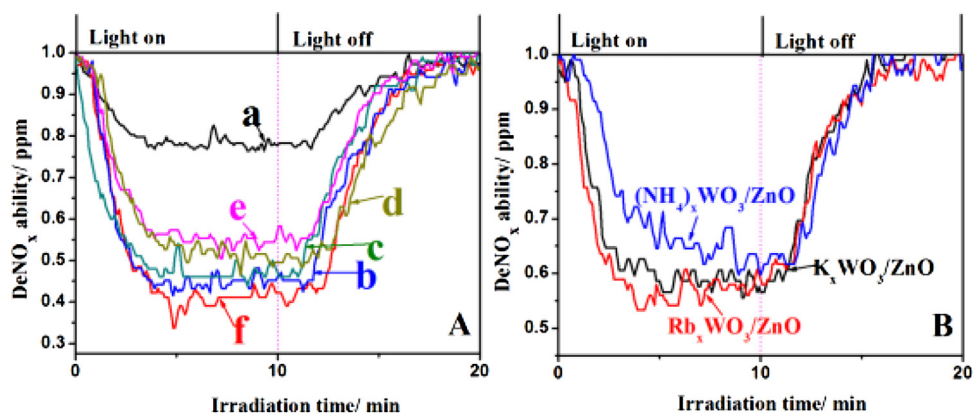
Fig. 9. Powder $DeNO_x$ ability of pure representative Rb_xWO_3 (a), Rb_xWO_3/ZnO (b), K_xWO_3/ZnO (c), $(NH_4)_xWO_3/ZnO$ (d), pure ZnO (f), P25 (e) powders (A) and the corresponding film photocatalytic activity for composites with respect to the mercury lamp irradiation time.
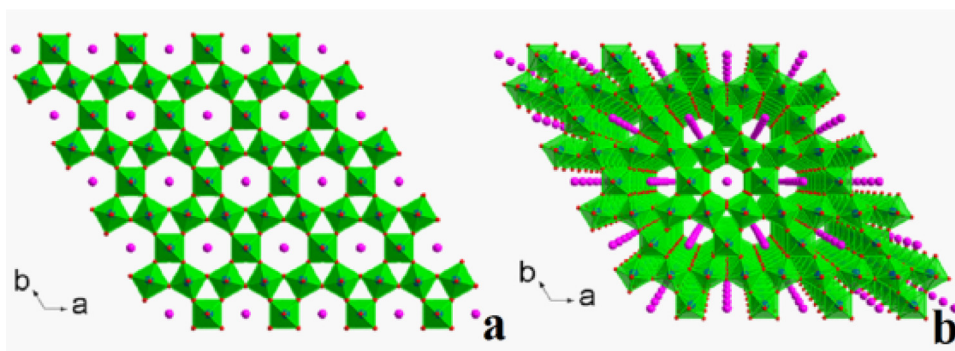
Fig. 10. Polyhedral representation of hexagonal tungsten bronzes M_xWO_3. The structure is viewed down the c-axis and the a is observed from normal projection and b is seen from central projection. Tunnel species M are represented by pink balls.

First of all, the excellent NIR light shielding property of M_xWO_3 is highly relevant to its hexagonal tungsten bronze crystal, which displays a typical tunnel structure. As shown in Fig. 10, the hexagonal tungsten bronzes consisted of a rigid tungsten-oxygen framework built up of layers including corner-sharing WO_6 octahedron, which are arranged in three and six-membered rings to form trigonal and hexagonal cavities, respectively. The layers were accommodated along the c-axis, finally producing the one-dimensional trigonal and hexagonal tunnels. Due to the large ionic radius of M ions, the M ions occupy the hexagonal cavities to form one-dimensional chains

of M ions and then loosely bounder to the cross-linked WO_6 octahedral framework. The maximum number of x was limited to 1/3 as M fully occupied the hexagonal cavities. When M occupies hexagonal sites, the t2g-block bands of the WO_3 lattice will be partially filled by the free electrons donated from the M atoms [32,33]. Moreover, combined with the above XPS analysis, it could be known that special W^{5+}, oxygen vacancies and free electrons originated from M incorporation present in the crystal of M_xWO_3, which will produce localized states just below the conduction band of M_xWO_3 as demonstrated in Fig. 11. Meanwhile, some free electrons from
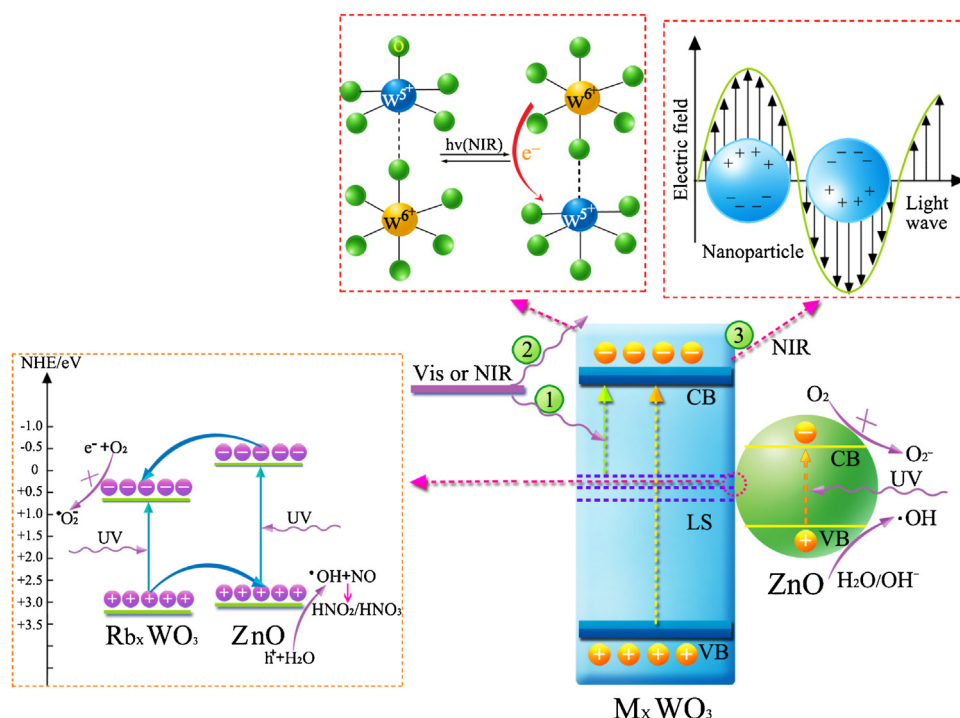
Fig. 11. Detail mechanism for the multifunctional properties of M_xWO_3/ZnO composites.

M atoms will also aggregate at the conduction band in addition to partially contributing to the localized states. In this case, when the natural solar light irradiates the M_xWO_3/ZnO composite film, the UV light in solar light will almost be blocked by M_xWO_3 and ZnO due to their widely intrinsic band gaps. While only small part of visible light in solar light will be absorbed due to defects and polaron effort. What's more, because of large intrinsic band gap and large amount contents of ZnO in the composite, the composite film could transmit most of VIS light and then present high brightness. As for NIR light, it could be clearly seen from Fig. 11 that the majority of it will be absorbed through two ways. The first way is the polaron transition containing process 1 and 2. In this way, the localized electrons would transfer from localized state to conduction band driven by absorbing suitable NIR light labelled as process 1. Besides, the localized electrons from reduced W^{5+} ions could also hop to the adjoining W^{6+} sites to absorb NIR light, named as process 2. In the first way, it mainly absorbed the short wavelengths of NIR light in the solar light (730–1100 nm). The second way is so-called localized surface plasma resonance (LSPR) as illustrated in Fig. 11 marked as process 3. The LSPR is induced from the aggregated free electrons in the conduction band when the incident NIR light energy is near to the oscillation frequency of free electrons. This way mainly shields the long wavelengths of NIR light in the solar light (1100–2500 nm) [12,14,29]. So through these two ways, the majority of NIR light in the solar light could be shielded by the composite film. In addition, the typical NIR and VIS light properties of M_xWO_3 were also closely related to the M concentration, particle size and morphology [18,19].

On the other hand, the absorbed UV light could be further used to excite redox reaction to decompose air or water pollution. In this work, the continuously NO gas was used as photocatalytic target and the Rb_xWO_3/ZnO series was represented to study the detailed photocatalytic mechanism. The band gaps of Rb_xWO_3 and ZnO were determined by Kubelka–Munk transformation based on the reflectance spectra as shown in Supporting information Fig. A.2(a) and (b), respectively. Regarding to the indirect band gap of Rb_xWO_3 and direct band gap of ZnO, the bandgaps of Rb_xWO_3 and ZnO were

approximately calculated to be 2.51 eV and 3.14 eV, respectively. Consequently, the conduction band (CB) and the valence band (VB) positions of Rb_xWO_3 and ZnO at the point zero charge could also be appropriately calculated referring to the following two equations [34,35]:
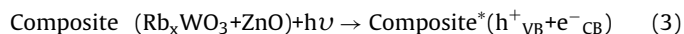
$$E_{CB} = \chi - E^e - 0.5E_g \tag{1}$$

$$E_{VB} = E_{CB} - E_g \tag{2}$$

Where E_{CB} and E_{VB} are related to the CB and VB positions of semiconductor, respectively; χ is the absolute electronegativity of the semiconductor; E_g is the band gap of the semiconductor; and E^e is assigned to the energy of free electron on the hydrogen scale. So based on the above obtained band gaps and two equations, the CB and VB positions of Rb_xWO_3 were determined to be ca. 0.69 eV and ca. 3.2 eV, respectively, and ca. −0.08 eV and 3.06 eV for ZnO, respectively, as presented in the left part of Fig. 11. In this case, a type II heterostructure can be formed between Rb_xWO_3 and ZnO in composite. When the composite Rb_xWO_3/ZnO is irradiated by UV light, the electrons in VB of Rb_xWO_3 and ZnO can be excited to CB of them as the incident energy of UV light is equal or larger than that of band gaps of Rb_xWO_3 and ZnO. Meanwhile, the photogenerated hole in the VB of Rb_xWO_3 will transfer to the VB of ZnO and the photogenerated electron in the CB of ZnO will move to the CB of Rb_xWO_3 owing to the variation of potentials, which is beneficial for the separation of photoinduced hole-electron pairs to improve photocatalytic activity. The photogenerated hole in the VB can then be further captured by water in the air to produce hydroxyl radicals $^\bullet OH$, which is one of the most active oxidation species. While in this system, it is very hard to produce $^\bullet O_2^-$ radicals by reducing O_2 with photogenerated electrons because the redox potential of $O_2/^\bullet O_2^-$ (−0.33 eV) is much more negative than those of the CB of Rb_xWO_3 (0.69 eV) and ZnO (−0.08 eV) [36]. Besides, Z. W. Zhao, et al. [37] have made a deep investigation about the photodegradation mechanism of NO gas according to the spin-trapping electron spin resonance (ESR) analysis, which is an effective technique to study the main active species accounting for the photocatalytic activity. It

was found that the •OH radical was the major active species for the photooxidation of NO gas in the presence of photocatalyst. So based on the aforementioned discussion and this research result, it could be deduced that when the target NO gas flow through the surface of composite with the irradiation of UV light, it would mainly be oxidized by photogenerated hole h$^+$ and •OH radicals to produce HNO$_2$ or HNO$_3$, which could be easily removed by rain [38]. The detailed photodegradation processes were proposed as follows:

$$\text{Composite} \ \ (\text{Rb}_x\text{WO}_3+\text{ZnO})+h\upsilon \rightarrow \text{Composite}^*(\text{h}^+_{\text{VB}}+\text{e}^-_{\text{CB}}) \quad (3)$$

$$\text{h}^+_{\text{VB}}(\text{ZnO})+\text{H}_2\text{O} \rightarrow \ \bullet \text{OH} + \text{H}^+ \quad (4)$$

$$\text{e}^-_{\text{CB}}(\text{Rb}_x\text{WO}_3) + \text{O}_2 \overset{\times}{\rightarrow} \bullet\text{O}_2^- \quad (5)$$

$$\text{NO} + 2\bullet\text{OH} \rightarrow \text{NO}_2 + \text{H}_2\text{O} \quad (6)$$

$$\text{NO}_2 + \bullet\text{OH} \rightarrow \text{NO}_3^- + \text{H}^+ \quad (7)$$

Therefore, referring to the above photocatalytic mechanism analysis, when the Rb$_x$WO$_3$ was employed to form a composite with ZnO, the photocatalytic degradation of NO by Rb$_x$WO$_3$/ZnO should be improved compared with those of solely Rb$_x$WO$_3$ and ZnO, due to the effective separation ability of photogenerated hole-electron pairs with heterostructure. However, the opposite results were presented in Fig. 9a, in which the NO degradation ability of ZnO was higher than that of composites. These abnormal phenomena was probably owing to that the specific surface area of composite was smaller than that of pure ZnO as described above, so that the relative amount of active sites on the surface were reduced; Secondly, the ratio of Rb$_x$WO$_3$ to ZnO in composite was probably not the optimal one to produce heterostructure effect. So optimizing the ratio of Rb$_x$WO$_3$ to ZnO in composite for photocatalytic activity and deeply mechanism investigation for this abnormal result will be our next work.

4. Conclusions

Series of M$_x$WO$_3$/ZnO (M = K, Rb, NH$_4$) nanocomposites have been successfully prepared by two brief steps of aqueous methods. They all presented promising optical properties, e.g. outstanding UV light blocking, nice VIS light transmittance and also excellent NIR light shielding. More importantly, Rb$_x$WO$_3$/ZnO exhibited the best NIR light shielding property with only 1/3 wt ratio of Rb$_x$WO$_3$ contents in composites as compared to other two composites. In addition, with increasing M$_x$WO$_3$ content and composite film thickness, the NIR light shielding capability of composite film could be significantly improved. Meanwhile, the composite film displayed excellent thermal stability for NIR light shielding below 100 °C. Under the simulated house system, the Rb$_x$WO$_3$/ZnO film decorated house presented excellent inner heat insulation capability, being superior to pure quartz one and even better than that of ITO one. On the other hand, ca.50% of toxic NO gas could be decomposed by composite and relevant film under the irradiation of UV light. The outstanding multifunctionality of composite are mainly assigned to the polaron transition, LSPR and fittable band gaps. Therefore, the proposed M$_x$WO$_3$/ZnO composites in this work could block not only harmful UV light, present high VIS light brightness for film and excellent heat insulation property, but also exhibit good air pollution decontamination performance, indicating a promising application in the area of energy-saving and environmental cleanup.

Acknowledgements

Appendix A. Supplementary data

Supplementary data associated with this article can be found, in the online version, at http://dx.doi.org/10.1016/j.apcatb.2016.08.030.

References

[1] C.S. Guo, S. Yin, P.L. Zhang, M. Yan, K. Adachi, T. Chonan, T. Sato, J. Mater. Chem. 20 (2010) 8227–8229.
[2] Z.T. Zhang, Y.F. Gao, H.J. Luo, L.T. Kang, Z. Chen, J. Du, M. Kanehira, Y.Z. Zhang, Z.L. Wang, Energy Environ. Sci. 4 (2011) 4290–4297.
[3] C.G. Granqvist, Adv. Mater. 15 (2003) 1789–1803.
[4] C.H. Ao, S.C. Lee, Chem. Eng. Sci. 60 (2005) 103–109.
[5] C.H. Ao, S.C. Lee, Appl. Catal. B: Environ. 44 (2003) 191–205.
[6] J.Y. Zheng, S.H. Bao, P. Jin, Nano Energy 11 (2015) 136–145.
[7] Y.F. Gao, S.B. Wang, L.T. Kang, Z. Chen, J. Du, X.L. Liu, H.J. Luo, M. Kanehira, Energy Environ. Sci. 5 (2012) 8234–8237.
[8] A.B. Huang, Y.J. Zhou, Y.M. Li, S.D. Ji, H.J. Luo, P. Jin, J. Mater. Chem. A 1 (2013) 12545–12552.
[9] C.S. Guo, S. Yin, Q. Dong, T. Sato, Nanoscale 4 (2012) 3394–3398.
[10] C.S. Guo, S. Yin, T. Sato, J. Am. Ceram. Soc. 95 (2012) 1634–1639.
[11] C. Bechinger, S. Ferrere, A. Zaban, J. Sprague, B. Gregg, Nature 383 (1996) 608–610.
[12] Y.C. Xin, H.J. Zhou, X.J. Ni, Y. Pan, X.L. Zhang, J.Y. Zheng, S.H. Bao, P. Jin, RSC Adv. 5 (2015) 57757–57763.
[13] H. Takeda, K. Adachi, J. Am. Ceram. Soc. 90 (2007) 4059–4061.
[14] K. Adachi, M. Miratsu, J. Mater. Res. 25 (2010) 510–521.
[15] M. Kanehara, H. Koike, T. Yoshinaga, T. Teranishi, J. Am. Chem. Soc. 131 (2009) 17736–17737.
[16] K.L. Purvis, G. Lu, J. Schwartz, S.L. Bernasek, J. Am. Chem. Soc. 122 (2000) 1808–1809.
[17] A. Hjortsberg, I. Hamberg, C.G. Granqvist, Thin Solid Films 90 (1982) 323–326.
[18] C.S. Guo, S. Yin, L.J. Huang, L. Yang, T. Sato, Chem. Commun. 47 (2011) 8853–8855.
[19] S. Yin, J. Ceram. Soc. Jpn. 123 (2015) 823–834.
[20] M. Yan, H.X. Gu, Z.Z. Liu, C.S. Guo, S.Q. Liu, RSC Adv. 5 (2015) 967–973.
[21] C. Santato, M. Odziemkowski, M. Ulmann, J. Augustynski, J. Am. Chem. Soc. 123 (2001) 10639–10649.
[22] H. Kato, K. Asakura, A. Kudo, J. Am. Chem. Soc. 125 (2003) 3082–3089.
[23] M. Setvin, U. Aschauer, P. Scheiber, Y.F. Li, W.Y. Hou, M. Schmid, A. Selloni, U. Diebold, Science 341 (2013) 988–991.
[24] K. Nakata, A. Fujishima, J. Photochem. Photobiol. C 13 (2012) 169–189.
[25] X.Y. Wu, S. Yin, D.F. Xue, S. Komarneni, T. Sato, Nanoscale 7 (2015) 17048–17054.
[26] C.S. Guo, S. Yin, L.J. Huang, T. Sato, ACS Appl. Mater. Interfaces 3 (2011) 2794–2799.
[27] S. Yin, M. Komatsu, Q.W. Zhang, F. Saito, T. Sato, J. Mater. Sci. 42 (2007) 2399–2404.
[28] D.L. Xu, D.F. Xue, H. Ratajczak, J. Mol. Struct. 740 (2005) 37–45.
[29] C.X. Yang, J.F. Chen, X.F. Zeng, D.J. Cheng, D.P. Cao, Ind. Eng. Chem. Res. 53 (2014) 17981–17988.
[30] Z.J. Gu, Y. Ma, T.Y. Zhai, B. Gao, W.S. Yang, J.N. Yao, Chem. Eur. J. 12 (2006) 7717–7772.
[31] D.G. Barton, M. Shtein, R.D. Wilson, D.G. Barton, S.L. Soled, E. Iglesia, J. Phys. Chem. B 103 (1999) 630–640.
[32] K.S. Lee, D.K. Seo, M.H. Whangbo, J. Am. Chem. Soc. 119 (1997) 4043–4049.
[33] T. Gao, B.P. Jelle, J. Phys. Chem. C 117 (2013) 13753–13761.
[34] Y.Y. Deng, Y.J. Chen, B.G. Chen, J.H. Ma, J. Alloys Compd. 559 (2013) 116–122.
[35] J.G. Yu, Y. Wang, W. Xiao, J. Mater. Chem. A 1 (2013) 10727–10735.
[36] Y.Y. Bu, Z.Y. Chen, C.J. Sun, Appl. Catal. B: Environ 179 (2015) 363–371.
[37] Z.W. Zhao, W.D. Zhang, Y.J. Sun, J.Y. Yu, Y.X. Zhang, H. Wang, F. Dong, Z.B. Wu, J. Phys. Chem. C 120 (2016) 11889–11898.
[38] X.Y. Wu, S. Yin, Q. Dong, C.S. Guo, H.H. Li, T. Kimura, T. Sato, Appl. Catal. B: Environ. 142–143 (2013) 450–457.